

Ultrafast quantum optics with attosecond control

Mohamed Sennary^{1,2†}, Javier Rivera-Dean^{3,4†}, Maciej Lewenstein³, Mohammed Th. Hassan^{1,2*}.

¹ Department of Physics, University of Arizona, Tucson, AZ 85721, USA.

² James C. Wyant College of Optical Sciences, University of Arizona, Tucson, Arizona 85721, USA.

³ ICFO–Institut de Ciencies Fotoniques, The Barcelona Institute of Science and Technology, Castelldefels (Barcelona) 08860, Spain.

⁴ Department of Physics & Astronomy, University College London Gower Street London WC1E BT, United Kingdom

*Corresponding author Email: mohammedhassan@arizona.edu.

†These authors contributed equally to this work.

Abstract

Modern Quantum optics largely remains quasi-stationary, far from intrinsic optical field timescales. Ultrafast quantum optics seeks to generate, shape, and measure quantum states of light on femtosecond and attosecond timescales. Here we introduce a quantum light field squeezer (QLFS) that enables the generation and attosecond control of ultrafast broadband squeezed light. Using degenerate four-wave mixing in a quasi-collinear focusing geometry, our approach overcomes conventional broadband phase-matching limits, producing intensity- and phase-squeezed states directly from few-cycle laser pulses. Our ultrafast quantum optical metrology reveals a time-dependent squeezing distribution across individual half-cycles of the electric field. Incorporating this time-dependent squeezing into strong-field simulations shows that the temporal redistribution of quantum uncertainty reshapes the high-harmonic emission. Moreover, by tuning the relative pulse delay and phase-matching angle, we achieve attosecond precision in controlling the squeezing characteristics by visualizing inferred effective Wigner representations of the quantum light field. Beyond characterization, we demonstrate that the quantum light-induced tunneling-current noise is sensitive to the nonclassical intensity-noise statistics of the driving squeezed light, with sub-femtosecond control. Together, these results extend the generation, control, and effective phase-space representation of squeezed light into the ultrafast and attosecond regime, opening new avenues for quantum optics in strong-field and solid-state systems.

Introduction

Quantum optics has long sought to control the quantum state of light and certify the presence of potential non-classical properties. Squeezed states—nonclassical light with reduced noise in one quadrature and increased in the other—have enabled breakthroughs in precision measurement and secure information transfer^{1,2}, yet their generation and manipulation have been limited to narrowband or quasi-continuous-wave regimes. Extending squeezing into the ultrafast domain is a critical milestone for next-generation quantum technologies, allowing access to natural dynamical timescales in matter³⁻⁶. Despite recent progress, current approaches are constrained by narrowband phase-matching requirements, operation primarily in the infrared, and the lack of metrology capable of resolving the time-dependent evolution of broadband nonclassical fields.

The generation of ultrafast bright squeezed vacuum (BSV) light has thus far been largely constrained to up-conversion frequency processes^{6,7}. This limitation arises because conventional

down-conversion schemes suffer from difficulties in sustaining broadband phase matching and preserving temporal coherence across the wide spectral distribution's characteristic of ultrafast pulses⁸. In contrast, up-conversion approaches enable broader phase-matching conditions, improved synchronization between pump and signal fields, and enhanced compatibility with high-speed detection technologies. For these reasons, they have become the dominant pathway for the generation of ultrafast squeezed states⁸. Thus, to date, the generation of ultrafast squeezed light has been restricted to squeezing in the phase quadrature (i.e. BSV), while the realization of intensity-squeezed ultrafast light pulses has remained out of reach. Despite these limitations, this advancement opens a new direction in research focusing on strong field quantum optics. The main research activities in this direction study the process of high-harmonic generation from a quantum optical perspective ⁹⁻¹⁵, use bright squeezed pulses to understand the properties of the generated XUV photons through HHG ^{10,16-21}, and control this nonlinear process characteristics towards quantum state engineering ^{20,22-27}. Moreover, on the detection side, single-photon-level measurements of ultrafast squeezed light remain hampered by current technological constraints. State-of-the-art single-photon detectors exhibit timing jitter far exceeding the femtosecond structure of the pulses, and typically lack the spectral resolution necessary to resolve broadband quantum correlations²⁸. Furthermore, losses, detector inefficiencies, dark counts, and mode mismatch with the local oscillator significantly diminish the observable degree of squeezing. These challenges underscore both the fragility of ultrafast squeezed states and the urgent need for advanced measurement strategies capable of faithfully capturing their quantum properties.

In our previous work³, we demonstrated the generation of ultrafast squeezed light spans new spectral regions (i.e. ultraviolet (UV), Visible, and near-infrared (NIR)) and presented the first real-time measurements of quantum-uncertainty dynamics in a broadband nonclassical field. That study focused on confirming squeezing and showing that its intensity fluctuations evolve with time. However, no mechanism for active state control, quadrant tuning, or full quantum-state reconstruction was explored.

In the present work, we uncover previously unobserved half-cycle time-dependent squeezing and its effect on strong-field interactions. Moreover, we introduce a fundamentally different capability: attosecond control and visualization of the squeezed state. By adjusting both the nonlinear phase-matching geometry and the relative arrival time of the interacting pulses, we directly engineer the squeezed quadrature and quantum uncertainty level with attosecond precision. Furthermore, using

a model-based analysis of the measured intensity fluctuations, we infer the evolution of an effective single-mode squeezed state and visualize its corresponding Wigner representation. This approach provides an intuitive phase-space representation of the quantum state dynamics consistent with the observed squeezing behavior. The underlying mechanism is explained in terms of manipulating the nonlinear generation time window, providing a physical basis for the observed control. Additionally, we study the quantum light-induced tunneling current and its encoding the squeezing level of light on the induced current noise, allowing this noise level control with attosecond resolution. These capabilities establish a practical path toward ultrafast quantum metrology and real-time quantum-state engineering, forming the foundation of ultrafast quantum optics.

1- Quantum light field squeezer

In our QLFS experiment (Fig. 1a), we used a coherent few-cycles near-infrared (NIR) laser pulse, centered at $\lambda = 790$ nm (Fig. 1b). This pulse was employed to generate squeezed light by the degenerate four-wave mixing FWM process, which becomes now a general platform for generating ultrafast quantum light pulse ²⁹. The broad bandwidth of the generated squeezed light highlights the ability of QLFS arrangement to overcome phase-matching limitations in typical quantum nonlinear optics. To confirm the squeezing produced by the FWM process, in addition to the shot-noise measurement (Fig. 1c), we evaluated the intensity uncertainty (ΔI) by calculating the integrated spectral intensity fluctuations and compared them with the corresponding ΔI of the input coherent light (Figs. 1d and e, respectively). To correlate ΔI with the phase uncertainty ($\Delta\Phi$), we further measured the phase fluctuations of the NIR pulses—both coherent and squeezed—relative to a reference visible pulse (500–700 nm), which partially overlaps with the NIR spectrum (~ 20 nm). The phase measurements are shown in Figs. 1f & g which indicates that the generated light exhibits intensity squeezing, since ΔI is reduced compared to the coherent input, hence the $\Delta\Phi$ quadrature exhibits the opposite trend. The uncertainty is driven by the intensity stability as we will prove later. This new metrology provides a broadband frequency-resolved intensity-fluctuation statistics as an indirect probe of nonclassical noise suppression. While distinct from conventional balanced homodyne detection, this approach provides experimentally accessible evidence consistent with quadrature squeezing under well-controlled conditions. In the QLFS, phase matching is inherently satisfied due to the quasi-collinear focusing geometry (see Fig. 1a), which allows the three input pulses to propagate quasi-collinearly with minimal spatial separation.

The beams are focused into the nonlinear medium with a small angle ($<3^\circ$). Accordingly, phase matching is achieved across the broadband spectrum of ultrafast pulses. This is demonstrated in Fig. 1b, where the nonlinear signal shows the same spectral span as the input beam. Hence, in addition to the NIR region (which is the focus of this study), the QLFS approach also enabled the generation of squeezed light in the UV and visible spectral regions³.

2- Time-dependent squeezing of the ultrafast squeezed light field for strong field physics

The broadband ultrafast squeezed light inherently comprises photons spanning a wide range of frequencies with different intensity and potentially spectral dispersion. Hence, each photon is likely to exhibit different degrees of squeezing, as predicted theoretically³⁰. Our metrology, complementary to conventional balanced homodyne detection, enables access to the intensity fluctuations as a function of frequency (ΔI_ω) across the broadband squeezed pulse. In our measurements, the pulse spectrum is recorded 2500 times, enabling statistical retrieval of the intensity uncertainty at each frequency component, ΔI_ω , which is plotted in Fig. 2a (focusing on the main spectrum of the pulse and avoiding the noisy edges). The frequency-resolved data reveal clear variations in ΔI across the broadband spectrum. These spectral dependencies likely arise from the nonuniform photon distribution across the ultrashort pulse spectrum combined with the wavelength-dependent nonlinear response of the dielectric medium during the FWM interaction. Notably, since ΔI_ω is extracted from 2500-shot statistics and benchmarked against coherent-state reference measurements, the observed spectral structure reflects genuine redistributions of quantum uncertainty rather than classical spectral noise.

To experimentally investigate that, we sampled the squeezed few-cycle pulse waveform (see Fig. 2b) using the dielectric reflectivity method we established earlier³¹⁻³³. The ΔI of four sampled scans of squeezed light are plotted in Fig. 2c in blue and black lines, respectively. Please note, we also used the same methodology to sample classical coherent fields (Fig. S1a) as reference measurement. The results show that the intensity uncertainty of the coherent light field is random, as expected, whereas that of the squeezed light is showing a quasi-similar trend each half-cycle over the entire field (Fig. 2c, and Fig. S1b). Remarkably, when zooming in on a single half-cycle of the squeezed field (see Fig. 2c inset), the squeezing level and ΔI are observed to vary within the half-cycle as a function of time. At intensity $I = 0$, ΔI is minimum (maximum phase uncertainty $\Delta\Phi$), and as the field intensity increases, ΔI increases until reaching the half-cycle intensity maximum (the phase squeezing reduced) where it shows a dip. The observed behaviors are

reproduced across multiple field-sampling measurements (Fig. S1b). Our time-domain field-sampling measurements reveal systematic sub-cycle variations in the inferred intensity-noise suppression of the squeezed field. These observations suggest a time-dependent redistribution of quantum uncertainty within individual optical cycles. Please note, the field sampling measurements nature might introduce certain noise which would affect the quantitatively assessment. However, our observation is focus on the relative intensity uncertainty for each half-cycle within the field and compare this behavior with the coherent light field qualitatively. Nonetheless, while the present measurements provide strong indications of sub-cycle squeezing dynamics, further confirmation using complementary field-sampling techniques , such as electro-optic sampling (EOS)³⁴⁻³⁷ and time-domain interferometric photoemission (TIPTOE)³⁸, which currently not available in our lab, will be valuable.

The time-dependent squeezing level of the electric field significantly affects the electron dynamics in strong-field interactions such as high-harmonic generation (HHG)¹⁶. When the squeezing varies in time, the generated spectra and the different harmonic orders have different second-order correlation function $g^{(2)}$ as observed experimentally²⁰. To investigate this effect theoretically, we performed simulations of HHG (see Methods) driven by five types of fields: (i) coherent light (reference), (ii) symmetric (time-independent) intensity-squeezed light, (iii) symmetric (time-independent) phase-squeezed light, (iv) time-dependent squeezed field 1, and (v) time-dependent squeezed field 2, with similar waveforms and cycle frequency (see Fig. S2). The corresponding HHG spectra appear in Fig. 2d. The intensity-squeezed field produce a spectrum with less cut-off the HHG spectrum coherent light field, whereas the phase-squeezed field (with large intensity fluctuations ΔI) and the two time-dependent squeezed fields yield spectra with higher cutoffs and broader bandwidths. Additionally, for the time-dependent squeezing level fields 1&2, the HHG plateau are blurring (Fig. 2d) due to the fluctuation of the intensity which slightly change the electron trajectory in the continuum and its return energy.

To further elucidate the underlying photon statistics nature, we calculated the $g^{(2)}$ values of the generated individual harmonics (Fig. 2e). For coherent and intensity-squeezed drivers, the odd harmonics all exhibit almost constant $g^{(2)} = 1$, compatible with coherent states of light. The time-dependent squeezed fields 1 and 2 driver yields odd harmonics with the lower orders (5, 7, 9) showing similar $g^{(2)}$ values that then the $g^{(2)}$ values vary up to $g^{(2)} = 2$ at higher harmonics, indicating super-Poissonian photon statistics. The phase-squeezed, which has the highest intensity

fluctuations over the entire field half-cycles, shows significant variation of $g^{(2)}$ values over the entire odd harmonic's orders.

The mechanism can be summarized as illustrated in Fig. 2f: time-dependent intensity uncertainty in the driving ultrafast field imprints itself onto the HHG process and is encoded in both the harmonic spectrum and photon statistics of the harmonics. The squeezed field modifies the instantaneous bending of the atomic potential, which determines the tunnel-ionization rate. Because tunneling is exponentially sensitive to the electric field, even small intra-cycle variations in intensity lead to large fluctuations in the release time and number of ionized electrons, producing strong shot-to-shot and sub-cycle variations in the electron wavepacket. If the intensity fluctuations differ between neighboring half-cycles (as in Fig. 2b), the potential bending becomes asymmetric with higher uncertainty of tunneling and recombination paths generating broader spectral structures, and potentially unstable attosecond emission. Such effects are expected for phase-squeezed or BSV light, which exhibit large intensity noise, whereas intensity-squeezed light—with reduced intensity fluctuations—should generate more stable XUV radiation. Remarkably, although fields 1 and 2 differ only in their time-evolving squeezing level over a half cycle, the resulting HHG spectra and the quantum statistical properties of the harmonics, $g^{(2)}$, are distinctly different. This demonstrates the significant impact of time-dependent squeezing on the strong-field interaction process.

3- Attosecond control and visualization of quantum states and Wigner function of squeezed ultrafast light pulse.

In our degenerate FWM nonlinear process, three identical beams of ultrafast laser pulses—originating from a single coherent input pulse—interact to generate a nonlinear light signal. The temporal window of nonlinear signal generation (T) determines the squeezing characteristics of the generated light (see illustration in fig. 3a). If the nonlinear generation time window is short (T is minimum), the nonlinear signal photons originate from the most intense overlap of the three pulses. In this case, intensity fluctuations are minimized, and the generated nonlinear signal light is squeezed in the intensity quadrature, with maximum phase uncertainty in accordance with the Heisenberg principle. Conversely, if the nonlinear signal is generated over a longer time window (T is maximum), the intensity exhibits larger fluctuations (ΔI is maximum), and the light is squeezed in the phase ($\Delta\Phi$). Thus, the interaction time window T depends on the phase-matching condition, the incident angle (θ), and the relative arrival time (τ) of the three input pulses. It is

important to note that the variation of τ is limited. At a critical delay, when one pulse is delayed too far relative to the other two, the temporal overlap becomes insufficient to generate a nonlinear signal. This critical delay depends on the pulse duration and the intensity of the input pulses. To study that, we control the relative arrival time of one pulse with respect to the other pulses involved in the FWM nonlinear process. This is achieved using a delay stage carries on the D-shaped mirrors in the QLFS (Fig. 1a). Two of the input beams are reflected from one fixed D-shaped mirror, while the third beam is reflected from a second D-shaped mirror mounted on a high-precision linear piezo stage. This configuration enables precise control of the arrival time of the third beam relative to the other two beams, with femtosecond and even attosecond resolution. Hence, the ΔI is measured at different delay time from 0 to -4 fs with 500 attosecond time steps (the estimated time jittering on our experiment setup is less than 100 as). The measurements at delays of 0, 1, 2, 3, and 4 fs are shown in Fig. 3b-f. These results demonstrate the change of the ΔI by changing T .

For visualizing the attosecond control of the ΔI fluctuations, we fitted our ΔI measurements to a theoretical value ΔI_{th} based on a displaced squeezed state³ of the form $|\phi\rangle = D(\alpha)S(r)|0\rangle$, where $D(\alpha) = \exp[\alpha\hat{a}^\dagger - \alpha^*\hat{a}]$ and $\hat{S}(r) = \exp[\frac{r}{2}(\hat{a}^2 - \hat{a}^{\dagger 2})]$ denote the displacement and squeezing operators, respectively. Here, α and (\hat{a}) are the photonic creation (annihilation) operators. From the measured data, we extract the variance ΔI^2 , which we compare with the theoretically predicted variance $\Delta I_{th}^2(\alpha, r)$ that depends on both the coherent state intensity α and the squeezing parameter r . The optimal parameters are obtained by minimizing the cost function (see Methods)

$$C(\alpha, r) = \left| \frac{\Delta I_{th}^2}{\langle I \rangle^2} - \Delta \bar{I} \right|, \quad (1)$$

such that $(\alpha^*, r^*) = \arg[\min_{\alpha, r} C(\alpha, r)]$.

Note that, consistent with the experimental definition of the uncertainties, the theoretical variance is normalized by the mean intensity $\langle I \rangle$. Using this procedure, we obtain for the optimal parameters $C(\alpha^*, r^*) \propto 10^{-15}$, which allows us to infer an effective single-mode state consistent with the measured intensity-variance statistics within the assumed displaced-squeezed-state model as ³⁹

$$W(x, p) = \frac{1}{\pi} \int_{-\infty}^{\infty} dy \langle x - y | \phi \rangle \langle \phi | x + y \rangle e^{i2py}. \quad (2)$$

It is worth noting that this theoretical fit is restricted to a single mode, which provides a quantitatively good approximation to the properties of the generated light³. Including additional,

uncorrelated modes would correspond to replacing the variance in Eq. (1) by $\Delta I_{th}^2 = \sum_i^N \Delta I_{th,i}^2$ in Eq. (1), where N denotes the total number of modes.

Accordingly, snapshots of the inferred effective Wigner representation associated with the fitted model parameters at different arrival times τ are shown in Fig. 3g. In addition, the estimated squeezing level in dB is plotted as a function of τ in Fig. 3h. By stacking all the snapshots in Fig. 3g, we generate an attosecond Wigner function movie that illustrates the real-time control of the squeezed light state (see Supplementary movie 1). The inferred effective Wigner representations are stable under the fitting procedure described, as confirmed by the analysis in the Methods section and the fitted parameters in Fig. S3. Moreover, the squeezing level of the ultrafast light pulse starts at maximum value at $\tau = 0$ fs and decreases observably for $\tau > 1$ fs as the generation time window T is increased, reaching minimum value at $\tau = 4$ fs. By tuning the relative arrival time and phase-matching geometry of the interacting pulses, we achieve attosecond-scale control over the nonlinear generation conditions that determine the effective squeezing strength and quadrature of the emitted light.

To quantify how the degree of squeezing evolves with the temporal overlap of the interacting pulses, we developed a phenomenological model that captures the dependence of the effective squeezing strength on the nonlinear generation time window T . This window represents the temporal duration over which the three optical fields overlap coherently within the nonlinear medium. As T changes with the relative delay τ between pulses, the nonlinear coupling strength and hence the measurable squeezing vary accordingly (see Methods). Using our model, we fitted the change of squeezing level as a function of the time delay and plotted in the black line shown in Fig. 3h. The results of the fitting (as explained in SM) indicating that the sub-femtosecond modification of the arrival time would have an observable change and control of the FWM nonlinear process and the squeezing level of the generated light.

Next, we switch between intensity and phase squeezing of the generated light, we change the phase matching condition in the FWM process by changing the incident angles (θ) of the three beams on the nonlinear medium. Then we performed the statistic measurements of the ΔI and the phase uncertainty ($\Delta\Phi$) (similar to the measurement done in Fig. 1e-f). The measurements of ΔI and $\Delta\Phi$ are shown in Fig. 4a-d, respectively. The statistical data reveal a clear trade-off between intensity and phase uncertainties and the that the phase is squeezed, and intensity is anti-squeezed, confirming the tunability and utmost control of the squeezed light quantum state. In time domain,

when the phase-matching angle θ is set to optimize phase squeezing, we study the underlying dynamics by measuring the ΔI as a function of the arrival time delay. Please note, the phase uncertainty ($\Delta\Phi$) cannot be traced at different delay steps since this would introduce a phase modulation not related to the $\Delta\Phi$ jittering. Hence, the change is indirectly investigated by measuring ΔI . A weak intensity squeezing is observed at perfect temporal overlap of the three beams ($\tau = 0$ fs). This intensity squeezing enhances as the arrival time τ increases since this delay compensates for the difference in the arrival time between the three pulses due to the change of the phase matching angle and the tilt of the nonlinear medium. The obtained snapshots of Wigner function at different time τ , from fitting the measured ΔI (following the same approach as in Fig. 3) are shown in Fig. 4e. The movie is provided in supplementary movie S2. The intensity squeezing level starts at the lowest level at $\tau = 0$ fs, then increases at higher τ until reaches maximum squeezing at $\tau = 4$ fs. These results show the femtosecond control of the squeezing states for the phase squeezed ultrashort laser pulses and supported with our fitting curve shown in black line in Fig. 4f (see Methods and SM).

4- Squeezed light-matter interaction

One of the ultrafast quantum optics research aims is to understand the interaction between quantum light and matter. In one of our previous work, we investigated light-induced electron tunneling using classical optical fields to demonstrate petahertz electronic switching (for experimental details, see Sennary et al.)⁴⁰. In the present study, we employ ultrafast intensity-squeezed light pulses to drive the electron tunneling process (see Fig. 6a) in a similar graphene–silicon–graphene heterostructure. Simultaneously, we measure the optical uncertainty ΔI of the squeezed light and the resulting statistical of current noise (ΔJ) induced by this squeezed light at different squeezing level (controlled by changing the T with 200 attosecond steps), simultaneously (see setup Fig. S4). The average statistics of 100 points is shown in Fig. 6b. These results show a evidence that the tunneling-current noise ΔJ is sensitive to the optical intensity-noise ΔI statistics of the nonclassical drive light. To confirm this current uncertainty is not related to the change of the induced squeezed light power (at different T), we measured the current statistics at different pump power of the squeezed light but at the same squeezing level (at $T = 0$ fs). The result is plotted in Fig. S5 and shows that the ΔJ is low at lower power, mostly dominated by electronics / thermal noise, then starts to increase as the power increases, indicating the onset of power-dependent noise. This behavior is different than that shown in Fig. 6b where ΔJ is minimum at $T=0$ where the power

of the squeezed light is maximum, confirming that the observed current noise variations originate from changes in the quantum state rather than from variations in the induced light power. Moreover, our results shown in Fig. 6b also demonstrate the capability of using our petahertz quantum current phototransistor⁴⁰ as a quantum sensor and control this sensing at attosecond time resolution.

We observe that the noise statistics of a light-induced tunneling current are sensitive to the nonclassical intensity fluctuations of the driving squeezed light, indicating that quantum optical noise properties can be transduced into an electronic observable and enhance the photo-induced current stability (see Fig. 6b), even if it is not reaching to shot-noise limit, where information encoded in the optical field quadrature is transferred to electronic degrees of freedom. In other words, the tunneling current acts as a sensitive probe of the optical intensity fluctuations, enabling readout of the state-dependent quantum noise of the ultrafast squeezed field. These results represent a step toward hybrid quantum interfaces in which nonclassical properties of light influence solid-state electronic dynamics. Moreover, the current noise and sensitivity can be controlled with sub-femtosecond resolutions paving the way to establish ultrafast quantum sensors and optoelectronics.

In summary, we have introduced and experimentally demonstrated an ultrafast quantum light field squeezer (QLFS) that enables the direct generation and active control of squeezed states of light across an ultrabroad spectral range. Using degenerate four-wave mixing in a quasi-colinear focusing geometry, our approach circumvents conventional broadband phase-matching limitations, producing intensity- and phase-squeezed states spanning the near-infrared, visible, and ultraviolet domains. By tuning the phase-matching angle, we achieve robust quadrature switching, while precise control of the relative pulse arrival times provides femtosecond-to-attosecond resolution in shaping the interaction window. Together, these capabilities establish a new level of tunability in quantum-state engineering, positioning the QLFS as a versatile platform for real-time manipulation of quantum light. Our metrology further accesses the intensity uncertainty of squeezed light in the frequency domain, revealing that this uncertainty varies temporally across the optical field and influences strong-field interactions such as high-harmonic generation. The observation of time-dependent squeezing within each optical cycle opens a new avenue in ultrafast quantum optics and the real-time evolution and control of nonclassical light fields on their natural temporal scales. Moreover, we demonstrate that nonclassical ultrafast light can control the noise

properties of a tunneling current, providing a first step toward hybrid quantum–electronic interfaces where electronic signals inherit quantum features of the optical field. Looking ahead, this methodology offers new opportunities for ultrafast quantum metrology, enhanced sensitivity in time-resolved spectroscopy, and next-generation quantum communication and computation. In addition, we present an experimentally accessible route to sub-femtosecond tuning of the effective squeezing characteristics, which opens a window into quantum light–matter interactions on their natural timescales, offering fresh insights into high-harmonic generation, entanglement dynamics, and ultrafast decoherence. By bridging ultrafast optics and quantum technologies, our results lay the foundation for a transformative new era of ultrafast quantum optics and quantum optoelectronics.

Methods

1- Quantum light field squeezer setup

In the QLFS configuration, illustrated in Fig. 1a, a coherent input laser beam of NIR 9-fs pulse (200 mW at repetition rate of 20 KHz), is divided into three identical sub-beams using a specially designed three-hole mask. The holes diameter is about 2 mm, but it can vary, allowing precise control over the intensities of the three beams. These beams are subsequently focused (beam size is about $50 \mu m$) and directed onto a nonlinear medium ($100 \mu m$ SiO₂) mounted on a gimbal stage by two identical concave (focal length=10 cm) D-Shaped mirrors, enabling flexible control of the incident angle (θ), the angle between the incident beam and the normal of the nonlinear medium. This arrangement allows the nonlinear interaction to produce a light signal ($2 \mu W$) with quantum squeezing properties. The angle θ is identified as the most critical parameter in the setup, as it governs the transition between intensity squeezing and phase squeezing. By varying θ , one can actively manipulate the quantum state of the generated light, enabling seamless conversion between quadrature states. The novelty of the QLFS arrangement lies in its ability to overcome the phase-matching problem, which is a common limitation in quantum nonlinear optics. By employing the three-beam geometry and fine angular control of the nonlinear medium, efficient FWM is achieved across a broad spectral range. Notably, this design allows the generation of squeezed light not only in the near-infrared (NIR) but also in the visible (Vis) and ultraviolet (UV) spectral domains. Moreover, the configuration opens the pathway for producing few-cycle and even attosecond-scale optical squeezed pulses, which are of considerable interest for ultrafast quantum optics and information processing ³. The arrangement in QLFS allows to control the arrival

time and nonlinear signal generation time window by control the delay of one of the three beams respect to the other beams by mounting the D-shape mirror on a high-precise piezostage which provide a linear motion resolution of few tens of attoseconds. We further introduce a novel broadband frequency-resolved statistical measurement that enables direct confirmation of the quantum nature of the light pulses and provide an access to the intensity uncertainty in the frequency domain.

2- Wigner function fitting

In experiments, the measured observable corresponds to the field intensity. Each measured shot $I(i)$ is compared to the mean intensity $\langle I \rangle_{exp}$ of the dataset, yielding the normalized deviation

$$\Delta I_i = \frac{1}{\langle I \rangle_{exp}} [I(i) - \langle I \rangle_{exp}], \quad (3)$$

from which we obtain a measure proportional to the variance,

$$\Delta \bar{I}^2 = \frac{1}{N_{iter}} \sum_{i=1}^{N_{iter}} \frac{[I(i) - \langle I \rangle_{exp}]^2}{\langle I \rangle_{exp}^2} = \frac{\Delta I^2}{\langle I \rangle_{exp}^2}, \quad (4)$$

where N_{iter} denotes the total number of experimental shots.

For a single mode displaced squeezed vacuum state, the theoretical intensity fluctuations read

$$\begin{aligned} \Delta I_{th}^2 &= \epsilon^2 [\langle a^{\dagger 2} a^2 \rangle - \langle a^{\dagger} a \rangle^2] \\ &= \epsilon^2 [|\alpha|^2 [2 \sinh^2(r) + 1] + 2 \sinh^2(r) [1 + \sinh^2(r)] - 2 \operatorname{Re}[\alpha^2] \sinh(r) \cosh(r)], \end{aligned}$$

while the expected value of the intensity is $\langle I \rangle_{th} = \epsilon^2 [|\alpha|^2 + \sinh^2(r)]$. To compare with the experimental, we define the cost function in Eq. (1) and minimize it numerically to determine the optimal parameters (α^*, r^*) . We focus on intensity- and phase- squeezed states, setting $\alpha \geq 0$ and $r \in \mathbb{R}$, and restrict the search to $r \in [-1.3, 1.3]$ and $\alpha \in [5, 50]$. A total of 1000 elements in each set $\{a\}$ and $\{r\}$ were used, where for each value of α a numerical optimization over r was done using each of the 1000 elements in the corresponding set as the initial value. This optimization was done via the BFGS-L algorithm, which is suitable for bounded parameter spaces.

The results for different time delays are shown in Fig. 3 & 4 for the two datasets. We find a broad range of single mode squeezed states compatible with the observed fluctuations, with the optimal cost function reaching values as low as 10^{-15} . Assuming identical experimental conditions across

all delays τ , the intensity α should remain constant. The green shaded area in Fig. S2 thus marks those values of α consistent with all delays, i.e., yielding $C(\alpha^*, r^*) \propto 10^{-15}$, defining upper and lower bounds for the level of squeezing compatible with the data.

Finally, for each optimal parameter (α^*, r^*) , corresponding to the curve with star markers in Figs. 3 (b) and 4 (f), we construct the quantum optical state $|\phi\rangle = D(\alpha^*)S(r^*)|0\rangle$ and compute its Wigner function $W(x, p)$ using Eq. (2). After the displacement $D(\alpha)$, which introduces only a trivial shift in phase space, the Wigner function of the resulting squeezed vacuum state reads

$$W(x, p) = \frac{1}{\pi} \exp[-e^{2r}x^2 - e^{-2r}p^2]. \quad (5)$$

In our analysis we reconstruct single-mode Wigner functions, which is appropriate because any Wigner function that can be visualized in two quadrature dimensions necessarily corresponds to a single optical mode. Each mode is fully described by its two conjugate quadratures, and the resulting Wigner representation provides a direct and intuitive visualization of squeezing through the relative deformation of these quadrature distributions. Although the experimental field is, in principle, a continuum of spectral-temporal modes, the number of effective modes contributing to the measurement is ultimately determined by the detection bandwidth and spectral resolution, which impose a natural discretization of the multimode structure. Importantly, any unaddressed multimode contributions—particularly in the presence of quantum correlations or mode-dependent squeezing—can reduce the observed squeezing of the reconstructed single mode. This occurs because unmeasured modes act as an effective loss channel, adding noise to the measured quadrature statistics. Our analysis and interpretation therefore focus on the dominant detected mode while acknowledging that multimode effects primarily manifest as a reduction in the measurable squeezing level rather than as artifacts in the reconstructed Wigner snapshots.

3- Modeling and fitting of the squeezing dependence on the nonlinear generation window

In our model, we assume that the effective squeezing parameter $r_{\text{eff}}(T)$ follows the overlap integral of three Gaussian pulses of characteristic interaction time σ , yielding

$$r_{\text{eff}}(T) = r_0 \frac{\sigma\sqrt{\pi}}{T} \operatorname{erf}\left(\frac{T}{2\sigma}\right), \quad (6)$$

where r_0 is the intrinsic squeezing parameter at perfect overlap ($T \rightarrow 0$), and erf denotes the error function. This function asymptotically approaches r_0 for small T and decays as $\sim r_0 \sigma/T$ for $T \gg \sigma$, consistent with the expected reduction of nonlinear gain for extended interaction durations.

The quadrature variance of the generated field is then given by

$$V_X(T) = (1 - \eta) + \eta e^{-2r_{\text{eff}}(T)}, \quad (7)$$

where η represents the total quantum efficiency, including all propagation and detection losses. The observable squeezing depth, expressed in decibels relative to a reference variance V_{ref} (e.g., the shot-noise level), is

$$S_{\text{dB}}(T) = -10 \log_{10} \left(\frac{V_X(T)}{V_{\text{ref}}} \right), \quad (8)$$

where positive values correspond to intensity noise suppression below the reference level.

In the intensity-squeezed configuration (Fig. 8), the three pulses overlap maximally at zero delay ($\tau = \tau_0$), and the effective interaction window increases approximately linearly with delay:

$$T(\tau) \propto |\tau - \tau_0|. \quad (9)$$

This relation yields a monotonic decrease of the squeezing level with increasing delay, in agreement with the experimental trend. Nonlinear least-squares fitting of Eq. (8) to the measured data allowed extraction of the parameters ($r_0, \sigma, \eta, \tau_0$), corresponding respectively to the intrinsic squeezing strength, effective interaction timescale, efficiency, and optimal temporal overlap.

To describe the phase-squeezed configuration (Fig. 4), we retained the same form of $r_{\text{eff}}(T)$ but modified the mapping between the generation window T and delay τ . In this geometry, the phase-matching condition causes the effective nonlinear interaction to become *more temporally localized* as delay is introduced; consequently, the squeezing increases with $|\tau - \tau_0|$. This reversed dependence is represented by

$$T(\tau) = \max (\varepsilon, T_0 - k |\tau - \tau_0|), \quad (10)$$

where T_0 denotes the maximal effective interaction window at optimal alignment, k quantifies the rate at which the overlap shortens with delay, and ε prevents numerical divergence at $T \rightarrow 0$. The corresponding phase-quadrature variance is

$$V_P(\tau) = (1 - \eta) + \eta e^{-2r_{\text{eff}}[T(\tau)]}, \quad (11)$$

and the phase-quadrature squeezing depth is

$$S_{\text{phase}}(\tau) = -10 \log_{10} \left(\frac{V_P(\tau)}{V_{\text{ref}}} \right). \quad (12)$$

Equations (5–7) accurately reproduce the experimental behavior observed in Fig. 4f, where phase squeezing increases with delay due to improved temporal localization of the nonlinear coupling. The fitted parameters ($r_0, \sigma, \eta, \tau_0, T_0, k$) respectively describe the intrinsic squeezing strength, interaction timescale, detection efficiency, temporal alignment, and geometric dependence of the effective generation window.

Together, these models demonstrate that both intensity and phase squeezing arise from the same underlying nonlinear mechanism, with the opposite trends emerging solely from geometry-dependent modulation of the generation window. This unified framework quantitatively links attosecond-scale temporal control to the quantum-state dynamics of ultrafast light.

4- High-harmonic generation calculations with squeezed light

To study the effect of the time depended squeezing of quantum light on strong field interaction, we performed HHG calculations follow an approach analogous to that adopted in previous works (see, e.g. [^{16,21,41}] and references therein). To account for the pulsed nature of the driving field, we consider a multimode source composed of five frequency components, at most two of which are prepared in a displaced squeezed vacuum state. Accordingly, we express the initial state of the driving field using the positive- P representation ⁴²,

$$\rho(t_0) = \bigotimes_{i=1}^3 |\bar{\alpha}_i\rangle\langle\bar{\alpha}_i| \bigotimes_{j=4}^5 \left[\int d^2 \alpha_j \frac{P(\alpha_j, \beta_j^*)}{\langle\beta_j^*|\alpha_j\rangle} |\alpha_j\rangle\langle\beta_j^*| \right] \bigotimes_{q \in HH} |0_q\rangle\langle 0_q|, \quad (13)$$

where the modes $i \in \{1, \dots, 5\}$ denote the driving field components, with the last two being potentially squeezed. Although several representations of the $P(\alpha, \beta^*)$ function exist, we choose a form that is explicitly positive, namely⁴³

$$P(\alpha, \beta^*) = \frac{1}{4\pi} \exp\left[\frac{|\alpha - \beta^*|^2}{4}\right] Q\left(\frac{\alpha + \beta^*}{2}\right), \quad (14)$$

with $Q(\alpha) = \pi^{-1} \langle \alpha | \rho | \alpha \rangle$ denotes the Husimi function of the corresponding driving field mode³⁹. In the absence of squeezing, when the five frequency components are prepared in coherent states with appropriately chosen intensity, we recover the vector potential $A(t) = -\int dt E(t)$ shown in Fig. S2a. For the different frequencies, we have chosen $\omega_1 = 0.057$ a.u. and $\delta = 0.013$ a.u., such that and $\omega_{2,3} = \omega_1 \pm \frac{\delta}{2}$, and $\omega_{4,5} = \omega_1 \pm \delta$. The corresponding electric field amplitudes are $E_1 = 0.053$ a.u., and $E_{2,3} = \left(\frac{2}{3}\right) E_1$, and $E_{4,5} = \left(\frac{1}{3}\right) E_1$.

The light-matter interaction between the driving field and the atomic system under consideration is governed by the Hamiltonian

$$H = H_{at} + e\mathbf{r} \cdot \mathbf{E} + H_{field}, \quad (15)$$

where H_{at} is the atomic Hamiltonian, which in our case corresponds to hydrogen atoms (ionization potential $I_p = 0.5$ a.u.). The term $e\mathbf{r} \cdot \mathbf{E}$ describes the light-matter interaction in the length gauge, with $\mathbf{E} = i\sum_j g(\omega_j)[a_j - a_j^\dagger]$ the electric field operator, $g(\omega_j)$ the light-matter coupling strength and $a_j^{(\dagger)}$ the annihilation (creation) operator acting on the j th optical mode. Finally, $H_{field} = \sum_j \hbar\omega_j a_j^\dagger a_j$ denotes the free-field Hamiltonian.

It can be shown that, under low-depletion conditions¹⁰ a solution to the Heisenberg equation of motion

$$i\hbar \frac{\partial \rho(t)}{\partial t} = -[H, \rho(t)], \quad (16)$$

can be approximately written as [^{16,41}]

$$\rho(t) \approx \prod_{i=4}^5 \int d^2\alpha_i \int d^2\beta_i \frac{P(\alpha_i, \beta_i^*)}{\langle \beta_i^* | \alpha_i \rangle} |\alpha\rangle \langle \beta^*| \otimes_{q \in HH} D_q(\chi_q(t; \alpha)) |0_q\rangle \langle 0_q| D_q^\dagger(\chi_q(t; \beta^*)), \quad (17)$$

where, we have represented $|\alpha\rangle = \otimes_{i=1}^3 |\bar{\alpha}_i\rangle \otimes_{j=4}^5 |\alpha_i\rangle$ and $|\beta\rangle = \otimes_{i=1}^3 |\bar{\alpha}_i\rangle \otimes_{j=4}^5 |\beta_i\rangle$. In the expression above, $D_q(\chi) = \exp[\chi a_q^\dagger - \chi^* a_q]$ denotes the displacement operator acting on the q th optical mode, with the displacement intensity given by¹³⁻¹⁵

$$\chi_q(t; \alpha) = \frac{i}{\hbar} g(\omega_q) \int_{t_0}^t d\tau \langle g | d_\alpha(t) | g \rangle e^{-i\omega_q \tau}, \quad (18)$$

where $\langle g | d_\alpha(t) | g \rangle$ denotes the time-dependent dipole moment. Within the strong-field approximation (SFA)^{44,45}, this quantity can be written as

$$d_\alpha(t) \propto \int_{t_0}^t dt' \int dp e^{-i\frac{1}{2} \int d\tau [p + A_\alpha(\tau)]^2 - iI_p(t-t')} d(p + A_\alpha(t)) E_\alpha(t') d^*(p + A_\alpha(t)) + c.c., \quad (19)$$

with $E_\alpha(t)$ and $A_\alpha(t)$ the expectation value of the electric-field and vector-potential operators, respectively, evaluated in the coherent state $|\alpha\rangle$. The numerical evaluation of $\chi_q(t; \alpha)$ was performed using the RB-SFA Mathematica package⁴⁶.

The two main quantities evaluated in this work, which involve only the generated harmonics, are the HHG spectrum $S(\omega_q)$ and the zero-delay second-order autocorrelation function $g_q^{(2)}(0)$. Both quantities can be written in terms of expectation values of observables O_q expressed as a normally ordered combinations of creation and annihilation operators, acting on the harmonic modes $q \in HH$, namely,

$$\langle O_q \rangle = \text{tr}[O_q \rho(t)] = \prod_{i=4}^5 \int d^2\alpha_i \int d^2\beta_i P(\alpha_i, \beta_i^*) o(\chi_q(t; \beta^*), \chi_q(t; \alpha)), \quad (20)$$

where we have defined

$$o(\chi_q(t; \boldsymbol{\beta}^*), \chi_q(t; \boldsymbol{\alpha})) \equiv \langle \chi_q(t; \boldsymbol{\beta}^*) | O_q | \chi_q(t; \boldsymbol{\alpha}) \rangle \prod_{q' \in HH - \{q\}} \langle \chi_{q'}(t; \boldsymbol{\beta}^*) | \chi_{q'}(t; \boldsymbol{\alpha}) \rangle. \quad (21)$$

More specifically, for the observables of interest we have

$$S(\omega_q) \propto \frac{\partial}{\partial \omega_q} \left[\sum_{q' \in HH} \hbar \omega_{q'} \langle \hat{a}_{q'}^\dagger \hat{a}_{q'} \rangle \right] \text{ and } g_q^{(2)}(0) = \frac{\langle a_q^{\dagger 2} a_q^2 \rangle}{\langle a_q^\dagger a_q \rangle^2}, \quad (22)$$

which we evaluate both in the so-called *classical limit*, also referred to as the *small single photon intensity* limit¹⁶. The relation between the coherent state intensity and the electric field strength, for a given mode of frequency ω , by $E_\alpha = 2g(\omega)\alpha$, where $g(\omega) \propto 1/\sqrt{V}$ and V denoting the quantization volume. In this limit, physical observables are evaluated under the requirement that $g(\omega) \rightarrow 0$ ($V \rightarrow \infty$) and $\alpha \rightarrow \infty$, such that the electric field strength remains finite. These two considerations are consistent with typical strong-field scenarios, where the driving field has an immense mean number of photons ($|\alpha|^2 \gg 1$), and occur in relatively large interaction volumes compared to atomic size ($V \gg 1$). Under this limit, it is found that^{16,41}

$$\langle O_q \rangle = \prod_{i=4}^5 \int d^2 E_{\alpha,i} \int d^2 E_{\beta,i} \lim_{V \rightarrow \infty} \left[\frac{1}{16g(\omega_L)^4} Q(\alpha_i, \beta_i^*) \right] o(\chi_q(t; E_{\boldsymbol{\beta}^*}), \chi_q(t; E_{\boldsymbol{\alpha}})), \quad (23)$$

where this limit does not explicitly affect explicitly affect $o(\chi_q(t; E_{\boldsymbol{\beta}^*}), \chi_q(t; E_{\boldsymbol{\alpha}}))$, as this quantity depends only on the electric field strength.

More specifically, for the case of squeezed states of light, it can be shown that⁴¹

$$\lim_{g(\omega_L) \rightarrow 0} \left[\frac{1}{16g(\omega_L)^4} Q(\alpha_i, \beta_i^*) \right] = \frac{1}{\sqrt{8\pi I_{squ}}} \exp \left[-\frac{(E_{\alpha,x} - \bar{E}_x)^2}{8I_{squ}} \right] \delta(E_{\alpha,y} - \bar{E}_y) \delta(E_\alpha - E_{\beta^*}) \quad (24)$$

where x is a variable running along the the antisqueezed optical quadrature, while y along the squeezed one. Furthermore, I_{squ} represents the squeezing contribution to the total intensity of the displaced squeezed vacuum states.

Figure 2d &e displays the results of this analysis. Figure 2d show the HHG spectrum for different driving fields. Specifically, time-dependent squeezed field 1, corresponds to a configuration in

which the driving field frequency components 4 and 5 are phase- and intensity-squeezed, respectively, while time-dependent squeezed field 2 considers the converse situation. For the phase-squeezed component, we set $I_{squ} = 0.5 \times 10^{-5}$ a.u., while for the amplitude-squeezed component $I_{squ} = 2.5 \times 10^{-5}$ a.u. Moreover, we also considered the case of pure phase and intensity squeezing (field strength set to be $\bar{E}=0.053$ a.u. Unlike the configurations shown in panel (a), these cases, pure phase and intensity squeezing, have been evaluated using a single-mode analysis, with a squared-sin envelope added to the electric field operator to achieve a similar waveform to the multimode cases (see Fig. S2 b,c)^{16,27}. Formally, within a multimode analysis line should establish an appropriate relation between the different squeezing strengths. However, for our five-frequency driving field pulse this becomes impractical, as the numerical analysis—where the integrals of the electric field strength are discretized using a total of 70 elements each—requires approximately two days to complete.

As can be observed in Figs. 2 (a) and (b), the HHG spectrum is slightly modified by the presence of squeezing in the different optical modes. While the extension of the HHG cutoff with respect to the coherent case (black curve) is not as pronounced as in the case of pure phase squeezing, the additional field fluctuations introduced by squeezing the field components 3 and 4 significantly affect the harmonic structure in the cutoff region, leading to a blurring of the harmonic peaks. In the plateau region, no resolved harmonic peaks are observed for any of the driving fields, as expected due to the interference of multiple electronic quantum orbits⁴⁷. However, for time-dependent squeezed field 1&2, the harmonic peaks do not become fully resolved even in the cutoff region, as the presence of bright squeezing in different optical modes of the driving field substantially modifies the temporal shape of the field, as shown in Fig. S2 d&e. Finally, Fig. 2 (c) displays the $g^{(2)}(0)$ which, except for the intensity squeezed and coherent cases, satisfies $g^{(2)}(0) > 1$ indicating super-Poissonian statistics, in agreement with recent results reported in the literature^{20,24-26}.

5- Squeezed light-induced quantum tunneling current experiment

In this experiment (setup is shown in Fig. S4), the main input squeezed light beam is divided by a beamsplitter (5:95) into two beams. The first reflected beam is focused onto a spectrometer. The integration of the spectra is used to calculate the relative standard deviation ΔI of the light intensity. The second beam, transmitted through the beam splitter, is focused by parabolic mirror ($f= 20$ cm) into the graphene-silicon-graphene junction. This squeezed light-induced tunneling

current in the phototransistor and this current (~ 4 nA at $T=0$ fs) is recoded by a current detector. The statistic measurement is performed by recording 20 points (repeated 5 times), then the relative standard deviation of the current is obtained ΔJ .

Acknowledgments:

This project is funded by the Gordon and Betty Moore Foundation Grant (GBMF 11476, <https://www.moore.org/grant-detail?grantId=GBMF11476>) to M. Hassan. This material is also based upon work partially supported by the NSF under award number 2537033 and the Air Force Office of Scientific Research under award number FA9550-22-1-0494.

J.R.D. and M.L. acknowledge support from: European Research Council AdG NOQIA; MCIN/AEI (PGC2018 0910.13039/501100011033, CEX2019-000910 S/10.13039/501100011033, Plan National STAMEENA PID2022-139099NB), project funded by MCIN/AEI/10.13039/501100011033 and by the “European Union Next Generation EU/PRTR” (PRTR-C17.I1), FPI); QUANTERA DYNAMITE PCI2022-132919, Fundació Cellex; Fundació Mir-Puig. Fundació Cellex; Fundació Mir-Puig.

Author contributions:

M.S. conducted the experiments and analyzed the data. J.R.D perform the theoretical calculations and fitting under the supervision of M.L. M.Th.H. conceived, supervised, and directed the study. All the authors discussed the results and their interpretations and wrote the manuscript.

Competing interests:

Authors declare that they have no competing interests.

References

- 1 Loudon, R. & Knight, P. L. Squeezed light. *Journal of modern optics* **34**, 709-759, (1987).
- 2 Andersen, U. L., Gehring, T., Marquardt, C. & Leuchs, G. 30 years of squeezed light generation. *Physica Scripta* **91**, 053001, (2016).
- 3 Sennary, M. *et al.* Attosecond quantum uncertainty dynamics and ultrafast squeezed light for quantum communication. *Light: Science & Applications* **14**, 350, (2025).
- 4 Kawasaki, A. *et al.* Real-time observation of picosecond-timescale optical quantum entanglement towards ultrafast quantum information processing. *Nat. Photon.* **19**, 271-276, (2025).
- 5 Braunstein, S. L. & van Loock, P. Quantum information with continuous variables. *Rev. Mod. Phys.* **77**, 513-577, (2005).
- 6 Asavanant, W. *et al.* Generation of time-domain-multiplexed two-dimensional cluster state. *Science* **366**, 373-376, (2019).
- 7 Barakat, I. *et al.* Simultaneous measurement of multimode squeezing through multimode phase-sensitive amplification. *Optica Quantum* **3**, 36-44, (2025).
- 8 Slusher, R. E., Hollberg, L., Yurke, B., Mertz, J. & Valley, J. Observation of squeezed states generated by four-wave mixing in an optical cavity. *Phys. Rev. Lett.* **55**, 2409, (1985).
- 9 Gorlach, A., Neufeld, O., Rivera, N., Cohen, O. & Kaminer, I. The quantum-optical nature of high harmonic generation. *Nature communications* **11**, 4598, (2020).
- 10 Stammer, P. *et al.* Entanglement and squeezing of the optical field modes in high harmonic generation. *Phys. Rev. Lett.* **132**, 143603, (2024).
- 11 Rivera-Dean, J. *et al.* Squeezed states of light after high-order harmonic generation in excited atomic systems. *Phys. Rev. A* **110**, 063118, (2024).
- 12 Lange, C. S., Hansen, T. & Madsen, L. B. Excitonic Enhancement of Squeezed Light in Quantum-Optical High-Harmonic Generation from a Mott Insulator. *Phys. Rev. Lett.* **135**, 043603, (2025).
- 13 Lewenstein, M. *et al.* Generation of optical Schrödinger cat states in intense laser-matter interactions. *Nat. Phys.* **17**, 1104-1108, (2021).
- 14 Rivera-Dean, J. *et al.* Strong laser fields and their power to generate controllable high-photon-number coherent-state superpositions. *Phys. Rev. A* **105**, 033714, (2022).
- 15 Stammer, P. *et al.* Quantum electrodynamics of intense laser-matter interactions: A tool for quantum state engineering. *PRX Quantum* **4**, 010201, (2023).
- 16 Gorlach, A. *et al.* High-harmonic generation driven by quantum light. *Nat. Phys.* **19**, 1689-1696, (2023).
- 17 Even Tzur, M. & Cohen, O. Motion of charged particles in bright squeezed vacuum. *Light: Science & Applications* **13**, 41, (2024).
- 18 Tzur, M. E. *et al.* Generation of squeezed high-order harmonics. *Physical Review Research* **6**, 033079, (2024).
- 19 Rasputnyi, A. *et al.* High-harmonic generation by a bright squeezed vacuum. *Nat. Phys.*, 1960-1965, (2024).
- 20 Lemieux, S. *et al.* Photon bunching in high-harmonic emission controlled by quantum light. *Nat. Photon.*, 1-5, (2025).
- 21 Wang, S., Lai, X. & Liu, X. Attosecond pulse synthesis from high-order harmonic generation in intense squeezed light. *Phys. Rev. A* **112**, L011102, (2025).

22 Theidel, D. *et al.* Observation of a displaced squeezed state in high-harmonic generation. *Physical Review Research* **7**, 033223, (2025).

23 Theidel, D. *et al.* Evidence of the Quantum Optical Nature of High-Harmonic Generation. *PRX Quantum* **5**, 040319, (2024).

24 Tzur, M. E. *et al.* Measuring and controlling the birth of quantum attosecond pulses. *arXiv preprint arXiv:2502.09427*, (2025).

25 Stammer, P., Rivera-Dean, J., Ciappina, M. F. & Lewenstein, M. Weak measurement in strong laser field physics. *arXiv preprint arXiv:2508.09048*, (2025).

26 Rivera-Dean, J., Petrovic, L., Lewenstein, M. & Stammer, P. Attosecond quantum optical interferometry. *arXiv preprint arXiv:2511.01097*, (2025).

27 Rivera-Dean, J. *et al.* Propagation of intense squeezed vacuum light in non-linear media. *arXiv preprint arXiv:2509.19608*, (2025).

28 Lvovsky, A. I. in *Photonics* 121-163 (2015).

29 Zimmerman, R. *et al.* Attosecond Control of Squeezed Light. *arXiv preprint arXiv:2512.17046*, (2025).

30 Kizmann, M. *et al.* Subcycle squeezing of light from a time flow perspective. *Nat. Phys.* **15**, 960-966, (2019).

31 Alqattan, H., Hui, D., Pervak, V. & Hassan, M. T. Attosecond light field synthesis. *APL Photonics* **7**, 041301, (2022).

32 Alqattan, H., Hui, D., Sennary, M. & Hassan, M. T. Attosecond electronic delay response in dielectric materials. *Faraday Discuss.* **237**, 317-326, (2022).

33 Hui, D. *et al.* Attosecond electron motion control in dielectric. *Nat. Photon.* **16**, 33-37, (2022).

34 Keiber, S. *et al.* Electro-optic sampling of near-infrared waveforms. *Nat. Photon.* **10**, 159-162, (2016).

35 Srivastava, A. *et al.* Near-petahertz fieldscopy of liquid. *Nat. Photon.* **18**, 1320-1326, (2024).

36 Virally, S., Cusson, P. & Seletskiy, D. V. Enhanced Electro-optic Sampling with Quantum Probes. *Phys. Rev. Lett.* **127**, 270504, (2021).

37 Adamou, D. *et al.* Quantum-enhanced time-domain spectroscopy. *Science Advances* **11**, eadt2187, (2025).

38 Park, S. B. *et al.* Direct sampling of a light wave in air. *Optica* **5**, 402-408, (2018).

39 Schleich, W. P. *Quantum optics in phase space*. (John Wiley & Sons, 2015).

40 Sennary, M. *et al.* Light-induced quantum tunnelling current in graphene. *Nature Communications* **16**, 4335, (2025).

41 Rivera-Dean, J., Stammer, P., Ciappina, M. F. & Lewenstein, M. Structured Squeezed Light Allows for High-Harmonic Generation in Classical Forbidden Geometries. *Phys. Rev. Lett.* **135**, 013801, (2025).

42 Drummond, P. D. & Gardiner, C. W. Generalised P-representations in quantum optics. *Journal of Physics A: Mathematical and General* **13**, 2353, (1980).

43 Drummond, P. D. & Chaturvedi, S. Quantum simulations in phase-space: from quantum optics to ultra-cold physics. *Physica scripta* **91**, 073007, (2016).

44 Lewenstein, M., Balcou, P., Ivanov, M. Y., L'huillier, A. & Corkum, P. B. Theory of high-harmonic generation by low-frequency laser fields. *Phys. Rev. A* **49**, 2117, (1994).

45 Amini, K. *et al.* Symphony on strong field approximation. *Rep. Prog. Phys.* **82**, 116001, (2019).

46 Pisanty, E. *RB-SFA: High-Harmonic Generation in the Strong Field Approximation via Mathematica*, <<https://github.com/episanty/RB-SFA>> (2020).

47 Salieres, P., Antoine, P., de Bohan, A. & Lewenstein, M. Temporal and spectral tailoring of high-order harmonics. *Phys. Rev. Lett.* **81**, 5544, (1998).

Figures and Figures legends

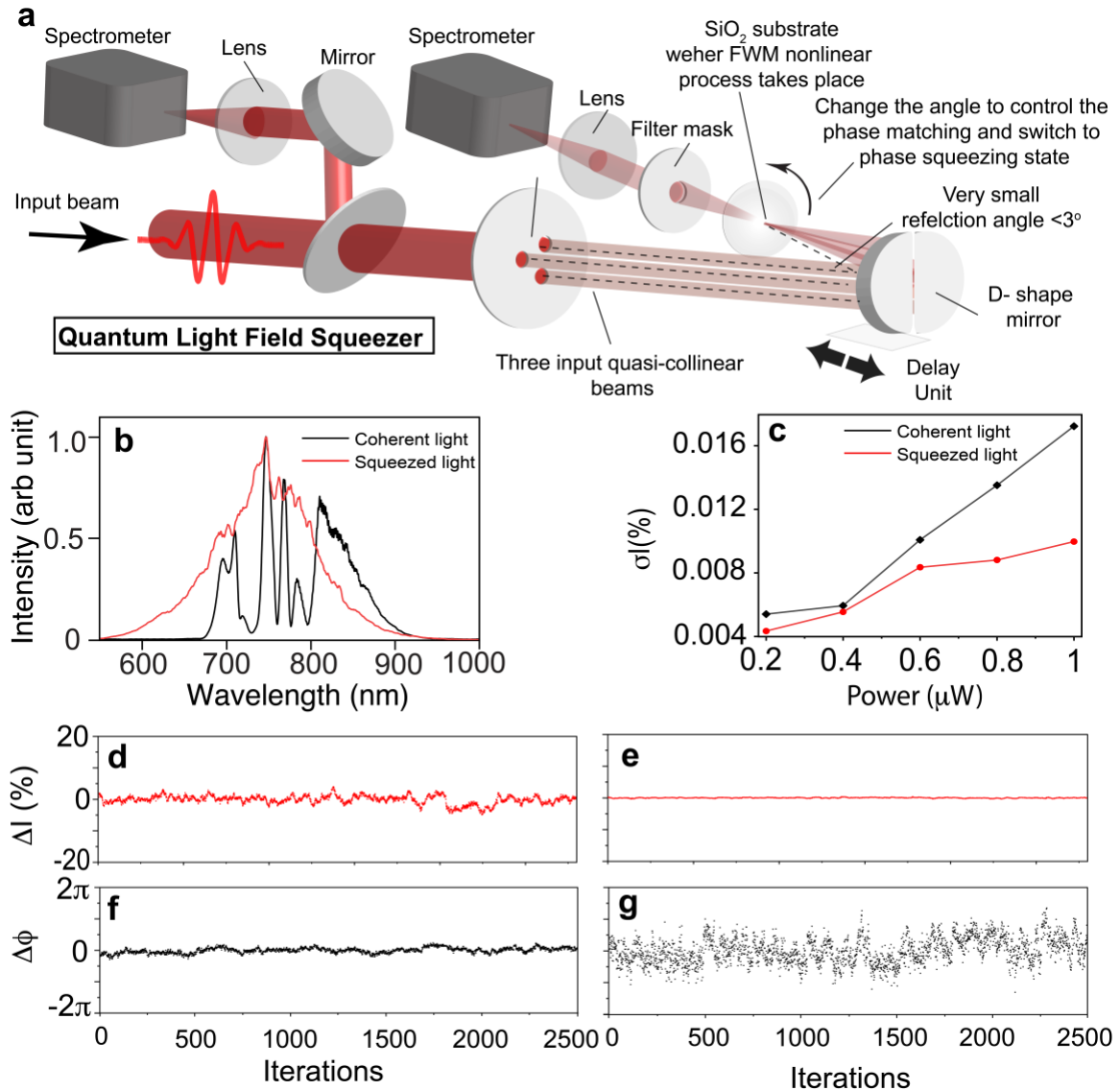


Figure 1 | Quantum Light Field Squeezer (QLFS) for generating broadband squeezed light. **a**, the QLFS setup illustration. In this setup, three beams emerge from the input beam incident on three-hole mask. These beams propagate quasi-colinear and focused by two D-shape mirrors on the fused silica where the FWM nonlinear process takes place to generate the squeezed light. the arrival time of the three beams on the fused silica is controlled by delay stage which carries one of the D-shaped mirrors. **b**, The broad spectrum of the input and the generated squeezed light in the NIR region. **c**, the shot noise measurement confirming the intensity squeezing of the generated nonlinear light signal from the FWM. **d-g**, the measured ΔI and $\Delta\Phi$ for the classic (**d & f**) and squeezed light (**e & g**).

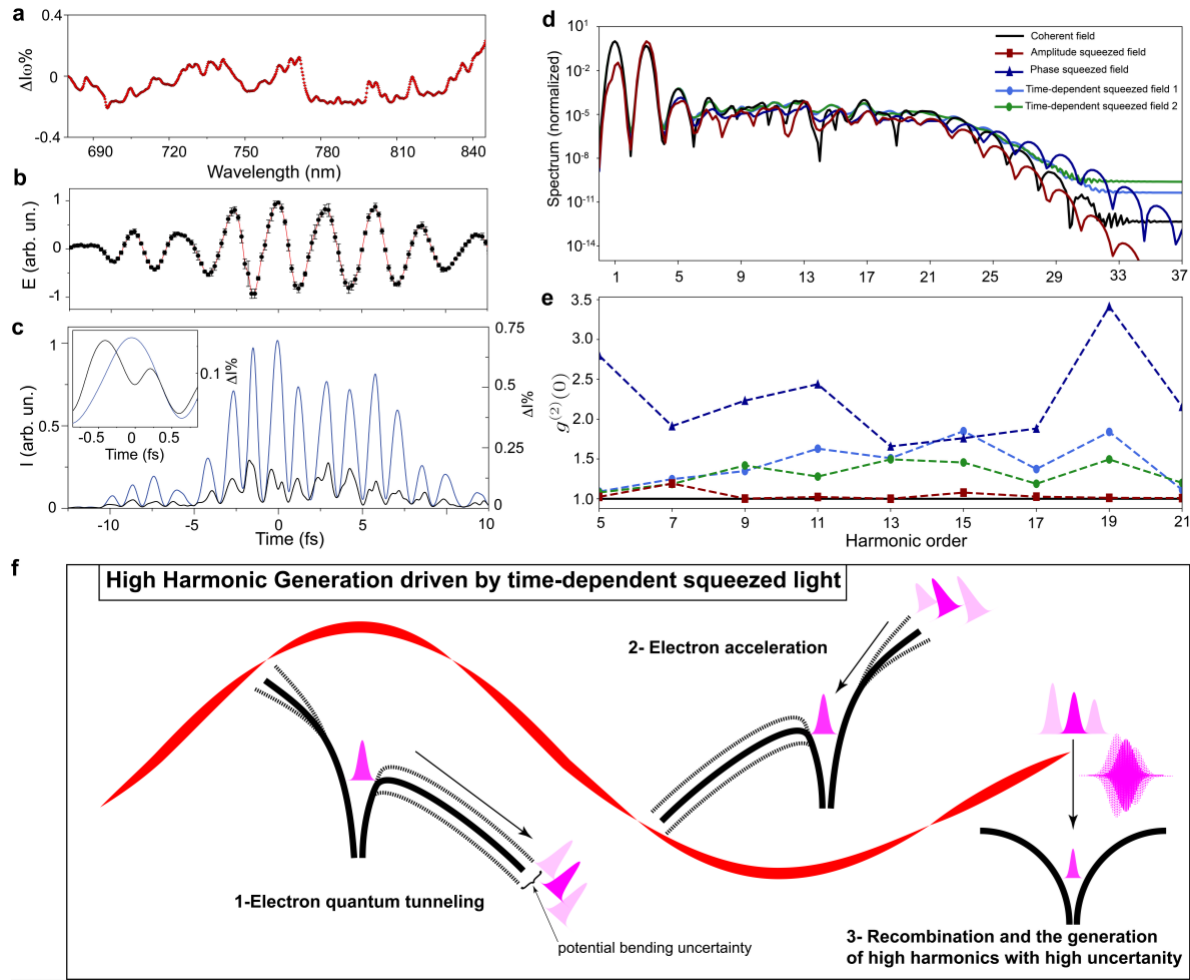


Figure 2 | Frequency and time-dependent squeezed light field. **a**, Measured frequency-dependent intensity uncertainty (of 2500 points) across the broadband spectrum of the NIR pulse. **b**, Average of four sampled squeezed-light fields, with error bars indicating the standard deviation of the field intensity. **c**, Field intensity and the corresponding relative ΔI of the squeezed field. The inset zooms into a single half-cycle, revealing both the asymmetry and the time-dependent evolution of ΔI within that half-cycle. **d** & **e**, The calculated HHG spectra and $g^{(2)}$ driven by coherent, intensity squeezed, phase squeezed, time-dependent squeezing field 1 and 2. **e**, Schematic illustrating how sub-half-cycle variations in the squeezing level of a driver pulse influence strong-field interactions (e.g. HHG), including both the squeezing and the trajectories of the resulting high harmonics.

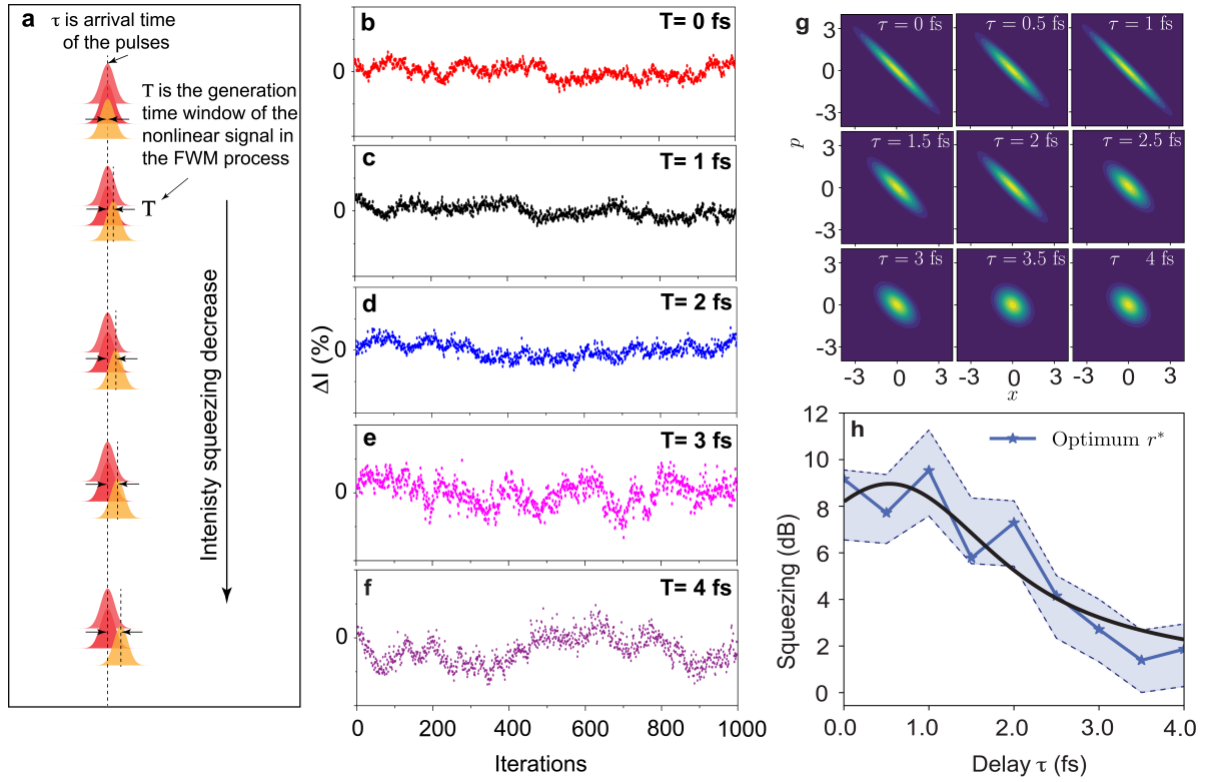


Figure 3 | Attosecond-resolved control and visualization of the Wigner-function dynamics of an intensity-squeezed ultrafast light pulse. **a**, illustration of the effect of the nonlinear signal generation time window on the generated light squeezing level. **b–f**, Modulation of the ΔI by varying the relative arrival time of one beam with respect to the other two (delay τ). Adjusting τ modifies the interaction time window T of the FWM process, enabling a continuous transition from maximum intensity squeezing ($T \approx 0 \text{ fs}$, $\tau = 0 \text{ fs}$) to reduced squeezing as T increases up to $\sim 4 \text{ fs}$. All the plots in b–f y-axis have the same scale range. **g**, Snapshots of the obtained Wigner functions at different delays, recorded from 0 to 4 fs in 500-attosecond steps, showing the continuous evolution of the squeezed quantum state. In these plots, x and p represent the optical quadrature, and for representational purposes, the distributions have been rotated by 45° relative to the p -axis. The full attosecond Wigner-function movie is provided as Supplementary Movie S1. **h**, Extracted squeezing level as a function of delay τ , revealing attosecond-precision control over the intensity quadrature. The blackline presents the fitting of the results.

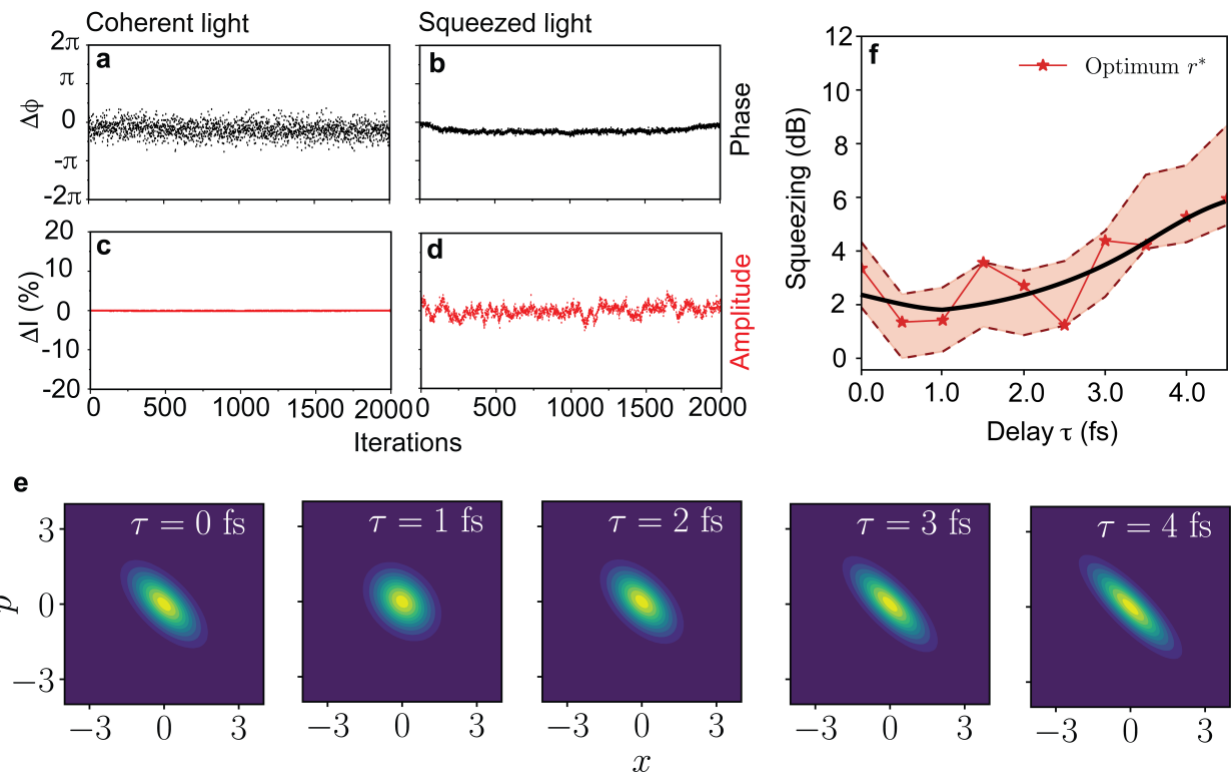


Figure 4 | Attosecond quantum uncertainty dynamics of phase-squeezing dynamics of ultrafast pulses. **a–d**, Measured phase variance ($\Delta\Phi$) and intensity variance (ΔI) for coherent light (a, c) and phase-squeezed light (b, d). The reduced phase noise and corresponding increase in intensity noise in panels b and d confirm active switching to phase-quadrature squeezing by tuning the phase-matching angle in the QLFS. **e &f**, Representative snapshots of the obtained Wigner functions and the corresponding squeezing level retrieved at different temporal delays τ (the blackline is the fitting of the results), demonstrating femtosecond-scale control over the phase-squeezed quantum state. In e plots, x and p denote the optical quadratures, and for illustrative purposes, the distributions have been rotated by 45° relative to the p -axis.

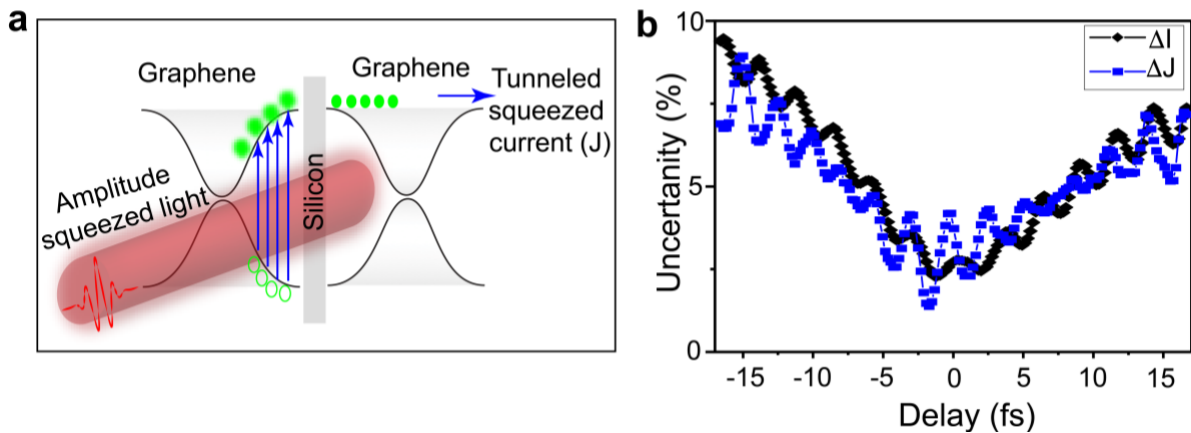


Figure 5 | Attosecond quantum light–driven tunneling-current noise transduction **a**, illustration of the quantum coupling between the driver squeezed light and the generated quantum tunneling current in Graphene-Silicon-Graphene phototransistor. **b**, the static measurements (average of 100 points) of the squeezed light intensity (ΔI) and the induced-tunneling current (ΔJ) uncertainties measured simultaneously.

Supplementary Information

Ultrafast quantum optics with attosecond control

Mohamed Sennary^{1,2†}, Javier Rivera-Dean^{3,4†}, Maciej Lewenstein³, Mohammed Th. Hassan^{1,2*}.

¹ Department of Physics, University of Arizona, Tucson, AZ 85721, USA.

² James C. Wyant College of Optical Sciences, University of Arizona, Tucson, Arizona 85721, USA.

³ ICFO–Institut de Ciencies Fotoniques, The Barcelona Institute of Science and Technology, Castelldefels (Barcelona) 08860, Spain.

⁴Department of Physics & Astronomy, University College London Gower Street London WC1E BT, United Kingdom

*Corresponding author Email: mohammedhassan@arizona.edu.

†These authors contributed equally to this work.

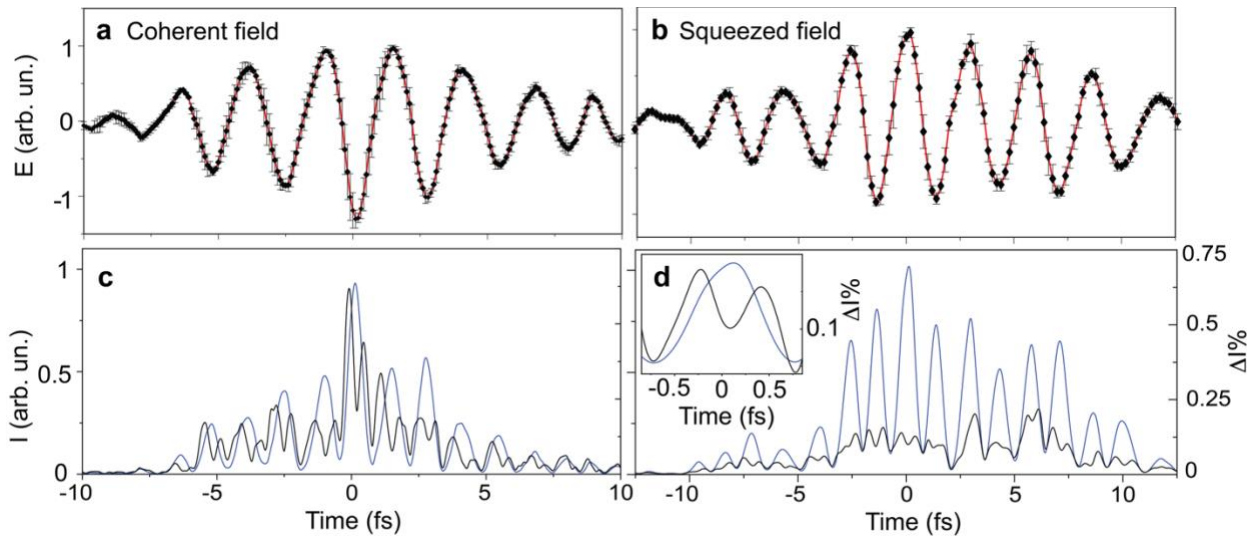


Fig. S1 | a & b, Average of four sampled coherent and squeezed-light fields, with error bars indicating the standard deviation of the field amplitude. **c & d,** Field intensity and the corresponding relative intensity uncertainty (ΔI) of the coherent and squeezed fields. Inset in d present the zoom in to illustrate the time-depended uncertainty within the half-cycle.

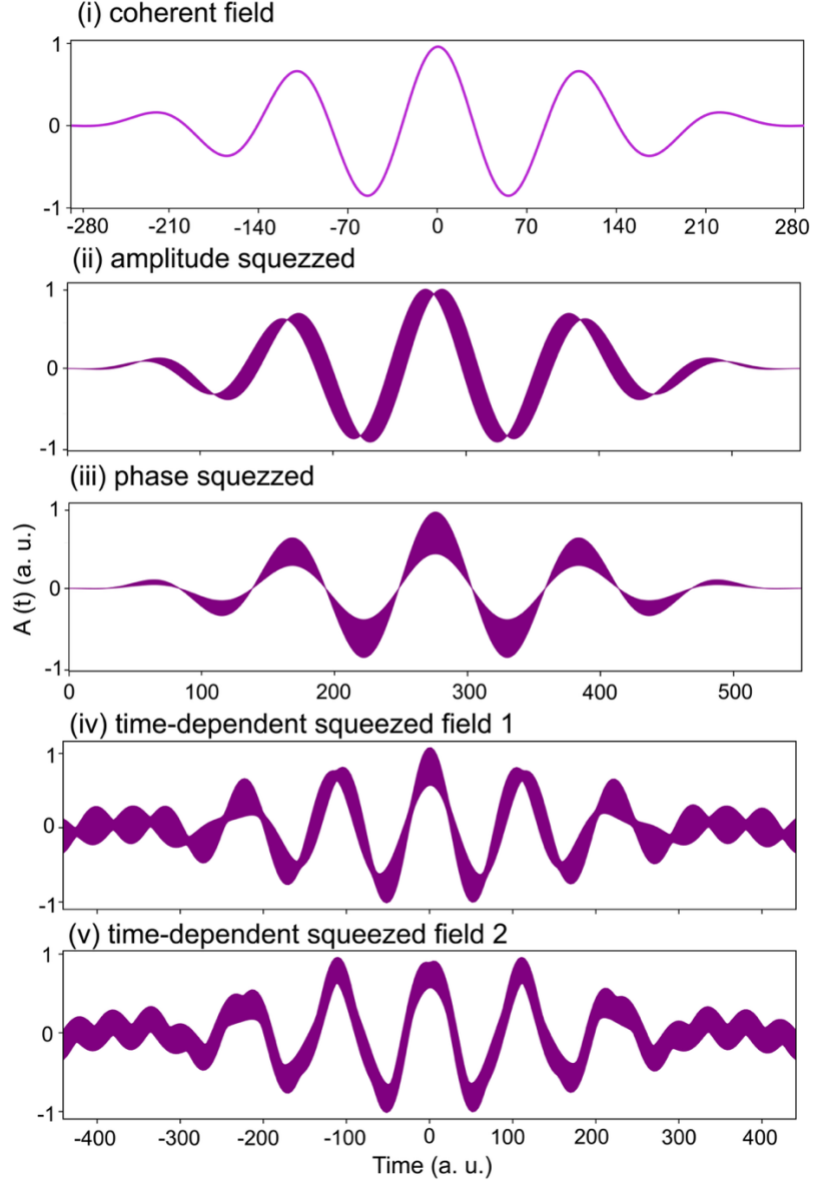


Fig. S2 | The five fields utilized for the HHG calculations shown in Fig. 2 d & e: (i) coherent light, the plot presents the vector potential corresponding to the quantum state described above in the absence of squeezing. For the different frequencies we have chosen $\omega_1 = 0.057$ a.u. and $\delta = 0.013$ a.u., such that $\omega_{2,3} = \omega_1 \pm \delta/2$ and $\omega_{4,5} = \omega_1 \pm \delta$. The corresponding electric field amplitudes are $E_1 = 0.053$ a.u., $E_{2,3} = (2/3)E_1$ and $E_{4,5} = (1/3)E_1$. (ii) symmetric (time-independent) amplitude-squeezed light, (iii) symmetric (time-independent) phase-squeezed light, (iv) time-dependent squeezed field 1, and (v) time-dependent squeezed field 2,

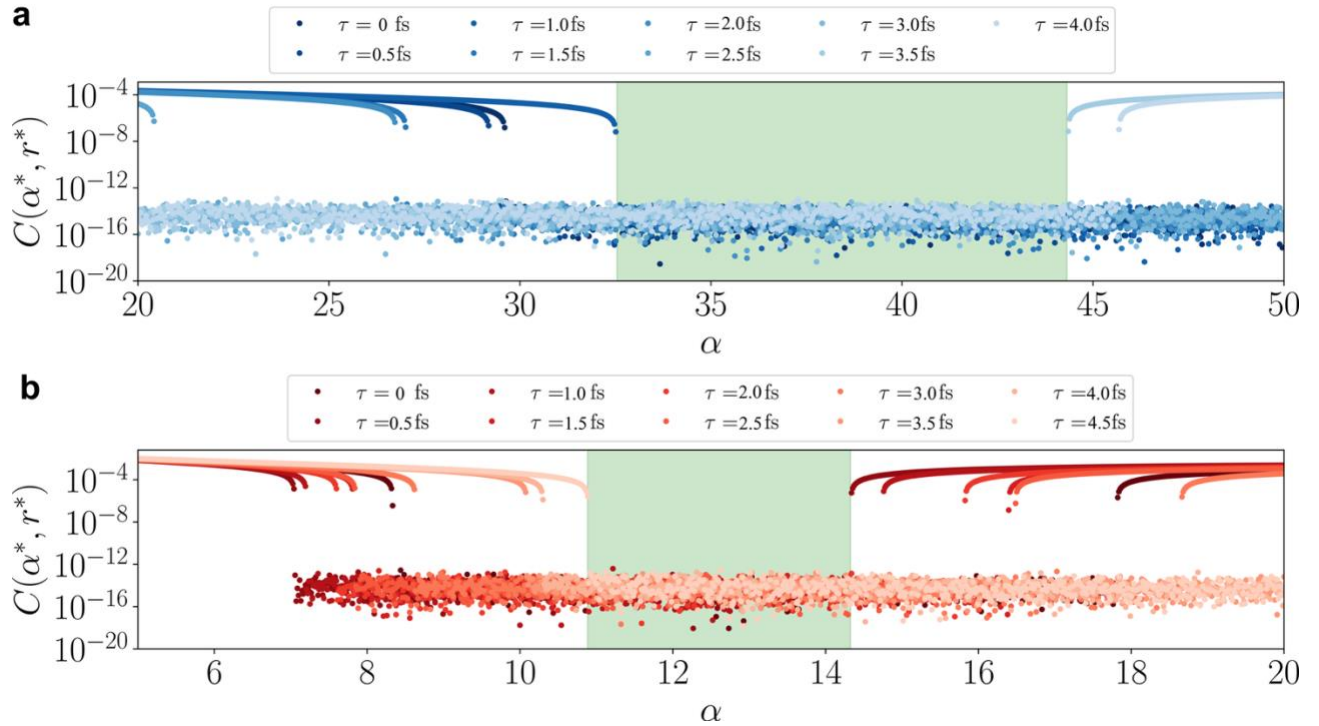


Fig. S3 Optimal value of the cost function as a function of α and for different time delays when evaluated on the different sets of experimental data. The green dashed region in both cases denote the region where optimal values as small as the numerical error are found for all delays.

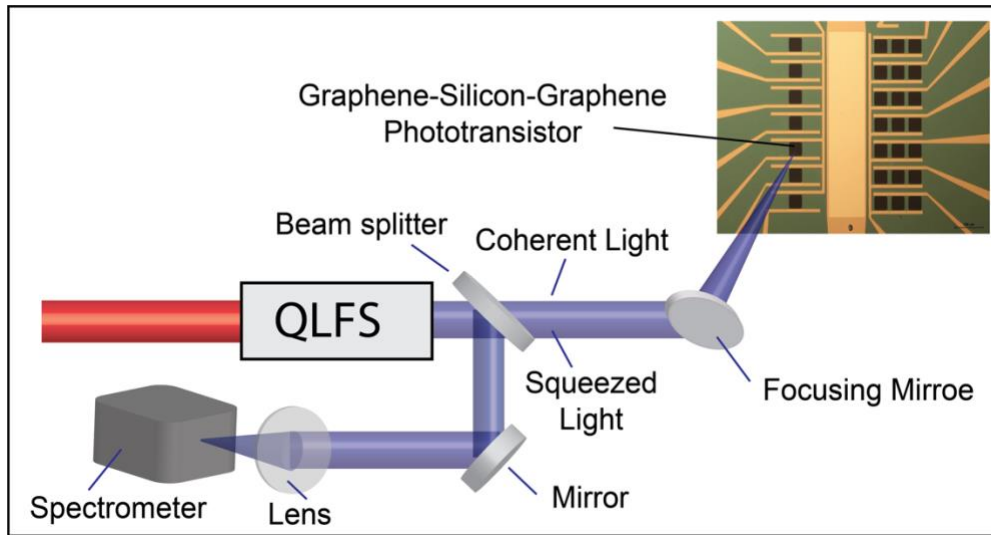


Fig. S4 | squeezed light-induced tunnelling current on graphene based phototransistor. The coherent light enters the QLFS to generate ultrafast squeezed light. This squeezed light is split by 5:95 beam splitter. The transmitted beam is focused by parabolic mirror into graphene transistor to generate a tunnelling current and to measure the current uncertainty (noise, ΔJ). The reflected beam is focused onto spectrometer to measure the optical intensity uncertainty (ΔI).

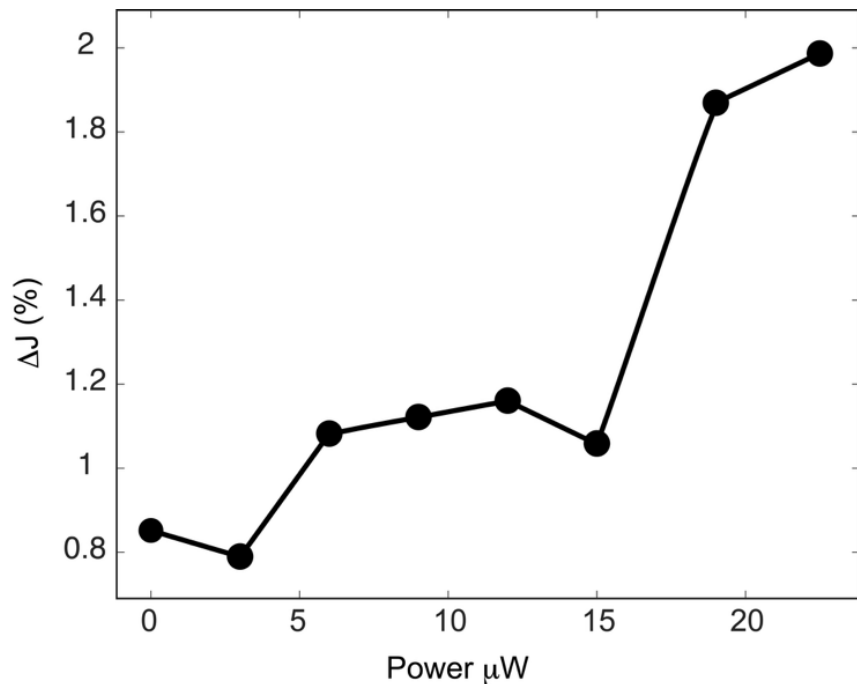


Fig. S5 | the measured ΔJ as a function of the squeezed pump light power.

Fitting of the amplitude squeezed change in real time

Fitting the squeezing model to the data in Fig. 3b yields $r_0 = 1.03$, $\sigma = 0.51$ fs, $\eta = 1.00$, and $\tau_0 = 0.53$ fs. The intrinsic squeezing parameter r_0 corresponds to an ideal maximum squeezing strength of approximately 9 dB, demonstrating that the degenerate four-wave-mixing process in the QLFS can, in principle, support strong nonclassical noise suppression under optimal conditions. The effective interaction timescale $\sigma \approx 0.5$ fs confirms that the relevant nonlinear coupling is confined to a sub-cycle temporal window of the few-cycle driving pulse, consistent with attosecond-resolved control of the quantum state. The efficiency factor $\eta = 1.00$ indicates that, within the uncertainty and assumptions of the model, the observed dependence is governed predominantly by the temporal evolution of the nonlinear generation window rather than by residual optical losses or mode mismatch. The fitted delay offset $\tau_0 \approx 0.53$ fs reflects a small, systematic timing shift required to reach optimal temporal overlap in the phase-matching geometry. Together, these parameters quantitatively support the interpretation that femtosecond-to-attosecond tuning of the relative arrival times directly tailors the nonlinear interaction window and, consequently, the magnitude of amplitude squeezing in the ultrafast regime.

Fitting of the phase squeezed field change in real time

Nonlinear least-squares fitting of Eqs. (10–12) to the experimental data in Fig. 4f yielded the parameters $r_0 = 1.104$, $\sigma = 0.614$ fs, $\eta = 0.853$, $\tau_0 = 1.0$ fs, $T_0 = 4.493$ fs, and $k = 1.146$. The extracted intrinsic squeezing parameter r_0 corresponds to the squeezing strength of approximately 1.104 dB at the perfect temporal overlap for phased squeezed light. The effective interaction timescale $\sigma = 0.614$ fs confirms that the nonlinear coupling is confined to a sub-cycle temporal window within the few-cycle driving pulse, consistent with attosecond-scale quantum control. The efficiency factor η saturates at unity within fitting uncertainty, implying that the observed dynamics are limited not by optical losses but by the intrinsic temporal evolution of the nonlinear overlap. The fitted delay offset $\tau_0 = 1$ fs corresponds to the temporal compensation required to achieve optimal phase amplitude in the tilted-beam geometry. Meanwhile, the maximal generation window $T_0 = 4.493$ fs and its reduction rate $k = 1.146$ quantify the geometric sensitivity of the nonlinear interaction: as the delay increases, the effective generation window shortens by roughly one femtosecond per femtosecond of delay, enhancing amplitude squeezing through temporal localization. Together, these parameters confirm that the attosecond control of the relative arrival

times directly modulates the nonlinear generation window and thereby governs both the magnitude and phase of quadrature squeezing in ultrafast quantum light.